Mean velocity profile in stably stratified turbulent channel flow

Kottурshettar, Sanath; Costa, Pedro; Pecnik, Rene

DOI
10.1017/jfm.2025.10972

Publication date
2025

Document Version
Final published version

Published in
Journal of Fluid Mechanics

Citation (APA)
Kotturshettar, S., Costa, P., & Pecnik, R. (2025). Mean velocity profile in stably stratified turbulent channel flow. *Journal of Fluid Mechanics*, *1025*, Article A44. https://doi.org/10.1017/jfm.2025.10972

J. Fluid Mech. (2025), *vol.* 1025, A44, doi:10.1017/jfm.2025.10972

Mean velocity profile in stably stratified turbulent channel flow

Sanath Kotturshettar[1], **Pedro Costa**[1] **and Rene Pecnik**[1]

[1]Process & Energy Department, TU Delft, Leeghwaterstraat 39, 2628 CB Delft, The Netherlands

Corresponding authors: Sanath Kotturshettar, s.b.kotturshettar@tudelft.nl; Rene Pecnik, r.pecnik@tudelft.nl

(Received 4 August 2025; revised 17 November 2025; accepted 18 November 2025)

The Monin–Obukhov similarity theory (MOST) is a cornerstone of atmospheric science for describing turbulence in stable boundary layers. Extending MOST to stably stratified turbulent channel flows, however, is non-trivial due to confinement by solid walls. In this study, we investigate the applicability of MOST in closed channels and identify where and to what extent the theory remains valid. A key finding is that the ratio of the half-channel height to the Obukhov length serves as a governing parameter for identifying distinct flow regions and determining their corresponding mean velocity scaling. Hence, we propose a relation to estimate this ratio directly from the governing input parameters: the friction Reynolds and friction Richardson numbers (Re_τ and Ri_τ). The framework is tested against a series of direct numerical simulations across a range of Re_τ and Ri_τ. The reconstructed velocity profiles enable accurate prediction of the skin-friction coefficient crucial for quantifying pressure losses in stratified flows in engineering applications.

Key words: stratified turbulence, channel flow

1. Introduction

Stratified turbulent flows are prevalent in environmental and engineering systems. Examples include atmospheric currents that affect pollutant dispersion, nutrient transport in oceans and fluid flows in energy conversion systems. In the case of stably stratified flows, where a lighter fluid overlies a heavier fluid, gravity acts to preserve the stratification, while turbulence promotes mixing of layers. The resulting flow behaviour is governed locally by the relative dominance of these competing mechanisms (Brethouwer *et al.* 2007; Zonta & Soldati 2018). Accurately predicting these flows is crucial in weather forecasting and determining key design parameters for engineering applications, such as the friction factor and the Nusselt number.

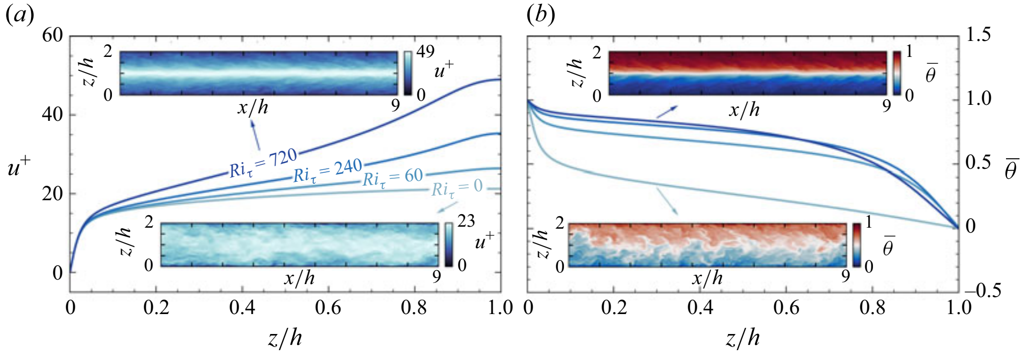

Figure 1. (*a*) Mean velocity profiles and (*b*) mean temperature profiles for friction Richardson numbers $Ri_\tau = \Delta\rho g h/\rho_0 u_\tau^2 = 0,\ 60,\ 240,\ 720$, represented with increasing darkness. Instantaneous contours at the mid-spanwise plane illustrate flow structures for neutral ($Ri_\tau = 0$) and stratified ($Ri_\tau = 720$) cases. All profiles and contours correspond to a friction Reynolds number $Re_\tau = \rho_0 u_\tau h/\mu_0 = 550$. In these governing parameters, u_τ is the friction velocity, ρ_0 and μ_0 denote the density and dynamic viscosity of the fluid, h is the half-channel height, g is the gravitational acceleration (pointing in the negative z direction) and $\Delta\rho$ is the imposed density difference across walls.

In wall-bounded turbulent flows, the presence of stable stratification leads to a reduction in both the skin-friction coefficient and the Nusselt number, as shown by Fukui, Nakajima & Ueda (1983). This reduction arises from the suppression of turbulent momentum and heat transport by buoyancy forces, especially away from the wall where shear is weak (Garg *et al.* 2000; Armenio & Sarkar 2002). Figure 1 illustrates this in instantaneous streamwise velocity and temperature contours for stratified and neutral (unstratified) channel flows. While velocity/temperature variations associated with near-wall flow structures can be observed in both cases, turbulent fluctuations can be severely damped in the outer region of the stratified channel due to buoyancy. As a result, the mean velocity and temperature gradients steepen near the channel centre; see the profiles near $z/h = 1$ (h is the half-channel height) in figure 1. Indeed, density gradients in the bulk can give rise to laminar internal gravity waves (IGWs) that interact with the turbulent regions of the flow (Iida, Kasagi & Nagano 2002), as visible in the contours of the stratified case in figure 1. Buoyancy effects suppress turbulence over a larger fraction of the channel compared with the atmospheric boundary layer (ABL), since turbulent shear linearly decreases from the wall, even leading to flow laminarisation at the centreline (Armenio & Sarkar 2002; Moestam & Davidson 2005; Garcia-Villalba & Del Alamo 2011). The underlying mechanism for the suppression of turbulent fluxes is the restriction of turbulent kinetic energy (TKE) redistribution across the channel height. Here, vertical turbulent mixing against a gravitational potential gradient results in the conversion of TKE into potential energy. This energy exchange can result in irreversible mixing of the density field, leading to TKE dissipation (Caulfield 2021).

Stably stratified wall-bounded turbulent flows have been extensively studied in the context of stable ABLs to describe the modulation of turbulent fluxes near the land surface. The most established framework used to predict the mean flow in this context is the Monin–Obukhov similarity theory (MOST), based on the seminal work of Monin & Obukhov (1954). In MOST, mean velocity gradients ($\mathrm{d}\overline{u}/\mathrm{d}z$) in the overlap region of a fully developed turbulent boundary layer subjected to stratification are related to the wall-normal distance (z) and the Obukhov length scale (L) (Obukhov 1971) as

$$\frac{\kappa z}{u_\tau}\frac{\mathrm{d}\overline{u}}{\mathrm{d}z}=\phi\left(\frac{z}{L}\right); \quad \text{with} \quad L=-\frac{u_\tau^3}{\kappa\ (g/\theta_0)\ q_w}, \tag{1.1}$$

where q_w is the surface heat flux, g/θ_0 is the buoyancy parameter and κ is the von Kármán constant. In this context, L estimates the height above which buoyancy starts to quench turbulent mixing, because buoyancy destruction of turbulence overwhelms shear production. The similarity function ϕ encapsulates the effect of stratification and is typically determined from atmospheric field data.

Subsequently, Nieuwstadt (1984) reasoned that the dynamics of stratified turbulence is better characterised by local rather than surface quantities, and introduced a scale based on local momentum and heat fluxes, $\overline{\tau}(z)$ and $\overline{q}(z)$. This results in a local Obukhov length scale

$$\Lambda(z)=-\frac{(\overline{\tau}(z)/\rho_0)^{3/2}}{\kappa\ (g/\theta_0)\ \overline{q}(z)}, \tag{1.2}$$

that extended the validity of MOST from the surface layer to the entire boundary layer (Nieuwstadt 1984; Holtslag & Nieuwstadt 1986; Sorbjan 1986). Although several refinements have been proposed over the years (Salesky, Katul & Chamecki 2013; Grachev *et al.* 2015; Li, Salesky & Banerjee 2016; Stiperski & Calaf 2023), the core principles of MOST remain remarkably valid. In striking contrast, its validity for describing internal wall flows remains largely unexplored.

Several detailed numerical studies have investigated the interaction between turbulence and stratification (see Zonta & Soldati 2018, for a review). Nieuwstadt (2005) performed the first direct numerical simulation (DNS) of open-channel flow driven by a constant pressure gradient, with stable stratification maintained by extracting heat from the lower wall. Building on these simulations, van de Wiel, Moene & Jonker (2012) and Donda *et al.* (2015) demonstrated that MOST can be applied to derive mean velocity profiles in open-channel flows. Differentially heated, closed turbulent channel flows with stable stratification have been studied since the early works by Garg *et al.* (2000) and Armenio & Sarkar (2002). Here, as we have seen, strong density gradients form near the channel centre, promoting the formation of IGWs (Iida *et al.* 2002). Garcia-Villalba & Del Alamo (2011) provided a detailed spectral analysis of these flows, demonstrating that the outer layer flow structures scale with Λ. More recently, Zonta, Sichani & Soldati (2022) proposed empirical correlations for predicting the friction coefficient and Nusselt number in stably stratified channel flows. Despite these advances, the applicability of MOST to describe the mean flow has not been explored.

The goal of this study is to address this gap and the following key question: How can MOST be extended to describe the mean flow of a stably stratified turbulent channel? In this work, we evaluate the validity of MOST in closed channels to trace the full mean velocity profile. To this end, we characterise the different flow regions considering the dominant balance between buoyancy and shear effects, and applying the corresponding local scalings. This involves not only deriving velocity scaling laws in the different regions, but also delineating the corresponding boundaries. Finally, we integrate the reconstructed mean velocity profile to estimate the skin-friction coefficient in stably stratified channel flow.

2. Computational campaign

We perform DNSs of stably stratified turbulent channel flows to develop a framework for describing their mean velocity profile, which is subsequently validated using the simulation data. The Navier–Stokes equations are solved in the low-Mach-number regime (Majda & Sethian 1985; Cook & Riley 1996), with a prescribed temperature difference of 1 %. This set-up ensures minimal variation in thermodynamic properties, enabling a reasonable comparison with cases in the literature that use the Oberbeck–Boussinesq approximation (see, e.g. Garcia-Villalba & Del Alamo 2011). The governing equations are

$$\frac{\partial \rho}{\partial t} + \frac{\partial \rho u_j}{\partial x_j} = 0, \tag{2.1}$$

$$\rho \frac{\partial u_i}{\partial t} + \rho u_j \frac{\partial u_i}{\partial x_j} = -\frac{\partial p}{\partial x_i} + \frac{\partial \tau_{ij}}{\partial x_j} + \rho g_i + f_i \delta_{i,1}, \tag{2.2}$$

$$\rho C_p \frac{\partial T}{\partial t} + \rho C_p u_j \frac{\partial T}{\partial x_j} = \frac{\partial}{\partial x_j}\left(\lambda \frac{\partial T}{\partial x_j}\right) + \frac{\mathrm{d}p_0}{\mathrm{d}t}, \tag{2.3}$$

where $\tau_{ij} = \mu(\partial u_i/\partial x_j + \partial u_j/\partial x_i - 2/3\ \partial u_k/\partial x_k\ \delta_{i,j})$. Here, p_0 denotes the spatially invariant thermodynamic pressure, while p represents the hydrodynamic pressure. The walls are maintained at fixed temperatures to enforce stable stratification. The arithmetic mean of the wall temperatures is chosen as the reference temperature at which the reference thermodynamic properties such as thermal conductivity (λ), heat capacity (C_p), dynamic viscosity (μ) and density (ρ) are evaluated. The density is related to temperature (T) via the ideal gas law ($\rho = p_0/RT$), where R is the universal gas constant. The gravitational acceleration vector g_i acts vertically downward, and f_1 represents the constant pressure difference driving the flow along the streamwise direction. Periodic boundary conditions are imposed in the streamwise and spanwise directions, while the no-slip condition is enforced at the walls. The equations were solved on staggered Cartesian grids, with velocities at cell faces and scalars at the cell centres. The convective and diffusive terms were discretised in space using a second-order, finite volume scheme (Costa 2018), and advanced in time using Wray's low-storage third-order Runge–Kutta method, with implicit treatment for wall-normal diffusion.

This set-up is characterised by a friction Reynolds number $Re_\tau = \rho_0 u_\tau h/\mu_0$, and a friction Richardson number, $Ri_\tau = \Delta\rho g h/\rho_0 u_\tau^2$ (Garg *et al.* 2000); ρ_0 and μ_0 denote the fluid density and dynamic viscosity at a reference temperature θ_0, h is the half-channel height and $\Delta\rho$ the bottom-to-top wall density difference. The DNSs were performed at $Re_\tau = 395$ and 550. Additionally, the data at $Re_\tau = 1000$ were obtained from Zonta *et al.* (2022). For each Re_τ, a range of Ri_τ was explored ($0 \leqslant Ri_\tau \leqslant 900$), at fixed Prandtl number $Pr = 0.71$. Figure 2 summarises the cases.

All simulations were conducted in a domain of dimensions, $L_x \times L_y \times L_z = 6\pi h \times 2\pi h \times 2h$, in the streamwise, spanwise and wall-normal directions, respectively. At $Re_\tau = 395$, nine different Ri_τ were simulated using a grid of $N_x \times N_y \times N_z = 1024 \times 512 \times 300$ points. On the other hand, eight different Ri_τ were simulated at $Re_\tau = 550$ using a grid of $N_x \times N_y \times N_z = 1536 \times 768 \times 480$ points. Uniform grid spacing was used in the periodic directions, while wall-normal grid stretching was applied to resolve the Kolmogorov length scale near the wall. Previous studies (e.g. Garcia-Villalba & Del Alamo (2011)) have indicated that increasing stratification does not affect the smallest turbulent scales, so grid resolution requirements remain unchanged with increasing Ri_τ. Simulations at higher Ri_τ were initialised using steady-state fields from the preceding lower Ri_τ case, following the strategy employed in earlier studies. Grid details of cases at $Re_\tau = 1000$ are available in Zonta *et al.* (2022).

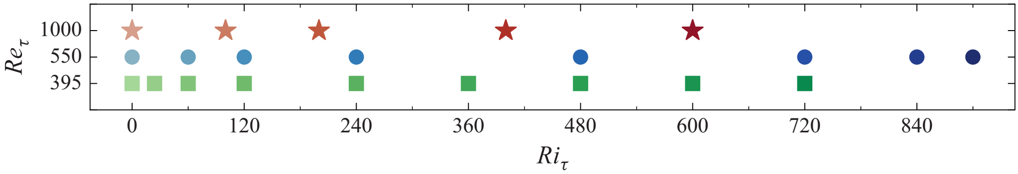

Figure 2. Summary of the parameter space sampled in the DNS database, with data at $Re_\tau = 1000$ from Zonta *et al.* (2022). Data for each case will be presented consistently with these marker colours.

3. Suitability of MOST for pressure-driven channels

While MOST was originally formulated for the ABL, we investigate its suitability in capturing the effects of stratification in turbulent channel flow. The applicability is assessed by examining the dependence of normalised velocity gradients on the wall-based (z/L) and local (z/Λ) stability parameters, as introduced in (1.1) and (1.2).

The function ϕ, commonly referred to as the stability correction function, is typically obtained empirically by fitting experimental data. The linear relations proposed by Webb (1970), Businger & Yaglom (1971)and Dyer (1974) provide a good fit for observations within the dry ABL, particularly under weak stratification. However, the functional form is not universal, with these studies reporting slightly different slopes for the linear relation, typically ranging between 4.5 and 5.5. Moreover, several alternative formulations for ϕ have also been proposed, including higher-order functions that reduce to a linear form under weak stratification but approach a constant value under strong stratification (Beljaars & Holtslag 1991; Chenge & Brutsaert 2005). Through their linear behaviour under weak and nonlinear corrections under strong stratification, these formulations recover the well-known 'z-less' region observed in the ABL (Nieuwstadt 1984). However, this region has not been observed in channel flows (Armenio & Sarkar 2002; Garcia-Villalba & Del Alamo 2011; Zonta & Soldati 2018).

In turbulent channel flows, the mean velocity (and, thus, its gradient) has been reported to increase with stratification. This is attributed to the reduction in turbulent shear stress under stable stratification. To represent this behaviour, we adopt the linear formulation proposed by Businger & Yaglom (1971), which captures the monotonic increase in velocity gradients with increasing stability. Figure 3 presents the dimensionless velocity gradients, $(\kappa z/u_\tau \, \mathrm{d}u/\mathrm{d}z)$, obtained from DNSs across a range of stratification levels as a function of the stability parameter: z/L in panel (*a*), and z/Λ in panel (*b*). The figure also shows the Businger relation $1 + 4.7\zeta$, where ζ is the stability parameter. Clearly, the local scaling captures the variation in velocity gradients more consistently than the wall-based scaling, particularly in representing the increase in gradient magnitude. Interestingly, although the Businger relation has been primarily validated within the 'constant-flux' layer, we find that it captures the velocity gradients reasonably well as long as turbulent shear remains the dominant mechanism and stratification effects are relatively weak $(z/\Lambda < 1)$. For $z/\Lambda > 1$, deviations from the linear relation become evident, with the Businger relation tending to overestimate the velocity gradients (see short dash-dotted lines in figure 3).

To improve the similarity hypothesis, in the context of ABL, Yokoyama, Gamo & Yamamoto (1979) proposed using 'z'-dependent surface parameters (e.g. $u_\tau(z) = u_\tau(1 - z/h)^\gamma$) that reliably estimate local fluxes. This method was subsequently adopted by Sorbjan (1986) and more recently by Gryning *et al.* (2007) and Shen *et al.* (2025). The exponent γ is determined empirically and varies across different studies. Following a similar approach, we apply a correction of the form $(1 - z/h)^\gamma$ to the Businger relation, with $\gamma = 1/2$. As shown in figure 3(*b*), the corrected relation captures the trend of the

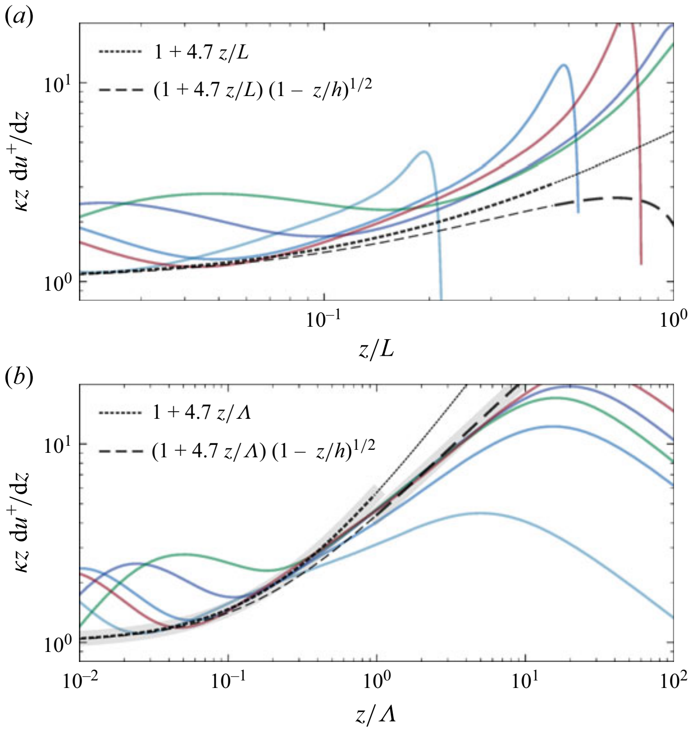

Figure 3. The dimensionless velocity gradients, ($\kappa z\ \mathrm{d}u^+/\mathrm{d}z$), obtained from DNSs across a range of stratification levels as a function of z/L in panel (a) and $z/\varLambda$ in panel (b). Increasing shades of blue correspond to $Ri_\tau = 60,\ 240,\ 720$ at $Re_\tau = 550$, the green line corresponds to $Ri_\tau = 720$ at $Re_\tau = 395$ and the red one to $Ri_\tau = 600$ at $Re_\tau = 1000$. These gradients are compared against the Businger relation, $1 + 4.7\ \zeta$, where ζ is the stability parameter.

velocity gradients reasonably well for $z/\varLambda > 1$, particularly in high Ri_τ cases, where this region is more distinct. Furthermore, the value of $\gamma = 1/2$ also aids analytical derivation through simplification of equations which will be discussed in the following sections.

In the region where $z/\varLambda > 1$, note that the current approach is equivalent to using a local friction velocity, $u_\tau(z) = u_\tau(1 - z/h)^{1/2}$, to normalise the velocity in (1.1) ($\kappa z\ \mathrm{d}u^+/\mathrm{d}z$), while maintaining the linear Businger relation. However, for the remainder of the article, we interpret this factor as a correction to the Businger relation rather than as an estimation of the local friction velocity, and use a mixing length model that consistently accounts for these variations.

4. Heat and momentum flux balance

Following Donda *et al.* (2015), $\varLambda$ can be expressed in terms of the wall-normal coordinate using the heat and momentum flux distributions. For pressure-driven turbulent channel flows, with walls at fixed temperatures, the mean total heat flux (q) is constant across the channel, while the total shear stress (τ) varies linearly

$$q(z) = \alpha \frac{\mathrm{d}\overline{\theta}}{\mathrm{d}z} - \quad \overline{w'\theta'} = q_w, \tag{4.1a}$$

$$\tau(z) = \mu \frac{\mathrm{d}\overline{u}}{\mathrm{d}z} - \rho_0 \overline{u'w'} = \tau_w \left(1 - \frac{z}{h}\right), \tag{4.1b}$$

where α is the thermal diffusivity, and the subscript 'w' denotes wall values. Substituting (4.1a) and (4.1b) into the definition of Λ (1.2) yields

$$\Lambda(z) = L\left(1 - \frac{z}{h}\right)^{3/2}, \tag{4.2}$$

with L the Obukhov length scale as given in (1.1). Approximating the turbulent flux in (4.1b) using the mixing length, we can write the stress balance in the well-known form

$$\nu \frac{\mathrm{d}\overline{u}}{\mathrm{d}z} + \ell_m^2 \left|\frac{\mathrm{d}\overline{u}}{\mathrm{d}z}\right| \frac{\mathrm{d}\overline{u}}{\mathrm{d}z} = u_\tau^2 \left(1 - \frac{z}{h}\right), \tag{4.3}$$

where $u_\tau = \sqrt{\tau_w/\rho_0}$ and $\nu = \mu/\rho_0$. This classical zero-equation model forms the basis for the proposed scaling laws. The mean velocity profile is naturally obtained by integrating (4.3) across the channel.

The mixing length (ℓ_m) is governed by the relative influence of buoyancy forces and turbulent shear. It is defined by scaling its value for pressure-driven turbulent channel flows in the neutral limit (ℓ_m^N), with the stability function ϕ that accounts for effects of stable stratification

$$\ell_m = \frac{\ell_m^N}{\phi}, \tag{4.4}$$

with ϕ being a function of z/Λ (recall the discussion in § 2). For ℓ_m^N, we adopt the mixing length reported by Pirozzoli (2014) for channel flows

$$\ell_m^N = \kappa z \left(1 - \frac{z}{h}\right)^{1/2}. \tag{4.5}$$

Note that, in (4.4), ℓ_m^N does not depend on the strength of stratification, and (4.5) is used across the entire channel. In contrast, the function ϕ accounts for stratification, and the stability correction should be used depending on the value of z/Λ, as discussed in § 2. Hence, based on the local balance between viscous and turbulent stresses, and the competing influence of buoyancy and shear, (4.3) can be simplified locally to identify distinct flow regions, as discussed in the next section.

5. Proposed mean velocity scaling

Figure 4 shows the typical distribution of viscous and turbulent shear stresses in a pressure-driven turbulent channel flow. Our analysis highlights five characteristic regions, as illustrated in figure 4(a), based on the distribution of the local stability parameter (z/Λ) and the relative magnitudes of viscous and turbulent stresses. For convenience of reporting, the regions are hereafter given descriptive names.

Closest to the wall, the classical viscous sublayer (I) (and the buffer layer) is unaffected by buoyancy forces as the strong shear dominates the stratification effects in this region. This is followed by a shear-dominated sublayer (II), where turbulent stresses dominate with minimal stratification effects. Further away from the wall, buoyancy effectively suppresses the larger eddies while the turbulent stresses are still much greater than the viscous stresses – a region termed here as the stratified outer region (III). Beyond lies the turbulent-viscous transition layer (IV), where viscous and turbulent stresses become comparable. Finally, from the channel centre, turbulence may vanish and lead to a laminar region, forming a viscous core layer (V) governed by viscous stresses. We now derive the mean velocity profile in these regions, excluding the well-established $u^+ = z^+$ scaling in the viscous sublayer.

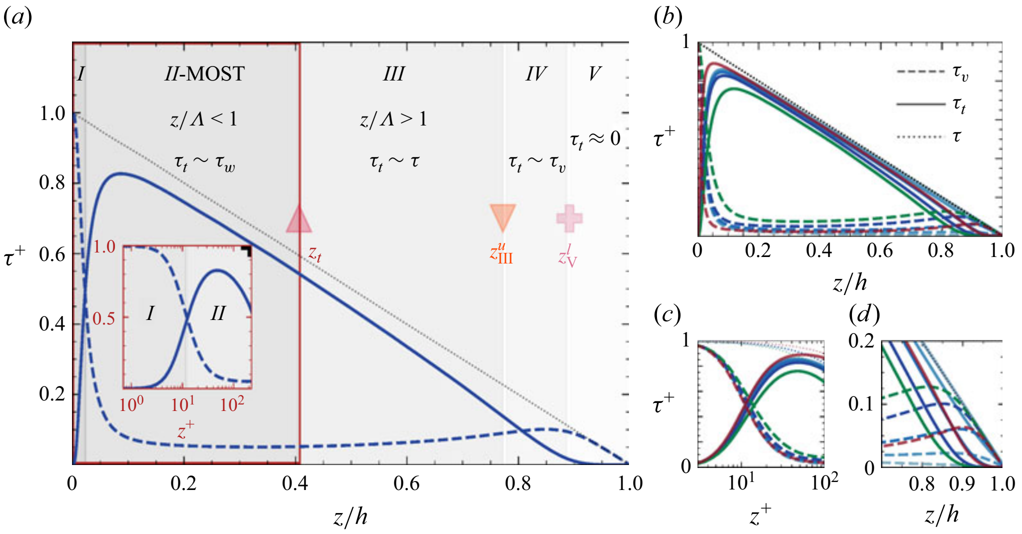

Figure 4. (*a*) Schematic illustrating the distinct regions in a stably stratified turbulent channel flow, classified based on the influence of stratification (quantified by $z/\varLambda$) and the relative contributions of viscous stress (τ_v) and turbulent stress (τ_t) to the total stress (τ). The identified regions are: viscous sublayer (I), shear-dominated sublayer (II), stratified outer region (III), turbulent-viscous transition layer (IV) and viscous core (V). The illustration corresponds to the case with $Ri_\tau = 720$ at $Re_\tau = 550$. (*b*) Stress profiles for various cases. Blue curves: $Re_\tau = 550,\ Ri_\tau = 0,\ 60,\ 240,\ 720$ (increasing darkness). Green: $Re_\tau = 395$, $Ri_\tau = 720$. Red: $Re_\tau = 1000$, $Ri_\tau = 600$ (Zonta *et al.* 2022). (*c*) Close-up of the profiles close in the near-wall region to illustrate the slow rise of turbulent stresses with increasing stratification. (*d*) Close-up near the centre of the channel, highlighting the drop-off of turbulent stresses to zero.

5.1. *Shear-dominated sublayer (II) – classical MOST*

Following the viscous sublayer, viscous stresses rapidly decrease while turbulent stresses increase, reaching a peak at approximately $z^+ \approx 30$ wall units (seen in figure 4*c*). In the shear-dominated sublayer, the local stability parameter $z/\varLambda$ is less than one, indicating that turbulent shear dominates over buoyancy effects. This is typically classified as the 'surface layer' in the ABL context, where the turbulent fluxes remain approximately constant and the classical MOST is applicable. In this region, (4.3) simplifies to

$$\ell_m \frac{\mathrm{d}\overline{u}}{\mathrm{d}z} = u_\tau \left(1 - \frac{z}{h}\right)^{1/2}. \tag{5.1}$$

The mixing length in the shear-dominated sublayer (II), denoted as ℓ_m^{II}, follows the formulation in (4.4). In this region, the effect of stable stratification is incorporated through the stability function represented by the linear Businger relation, $\phi = 1 + 4.7\zeta$, where $\zeta = z/\varLambda$ corresponds to the local stability parameter (recall figure 3 and the discussion thereabout). Hence, the mixing length is given by

$$\ell_m^{\mathrm{II}} = \frac{\ell_m^N}{\phi} = \frac{\ell_m^N}{1 + 4.7\,\zeta} = \frac{\kappa z}{1 + 4.7\,\zeta}\left(1 - \frac{z}{h}\right)^{1/2}; \qquad \zeta = \frac{z}{\varLambda}. \tag{5.2}$$

Figure 5 presents a comparison between the mixing length measured from DNS data, $(-\overline{u'w'})^{1/2}/(\mathrm{d}\overline{u}/\mathrm{d}z)$, and the expression given by (5.2). A good agreement is observed in the region where turbulent shear dominates (i.e. $z/\varLambda < 1$, see the fine dashed lines). The expression begins to deviate from the DNS profile when buoyancy effects become

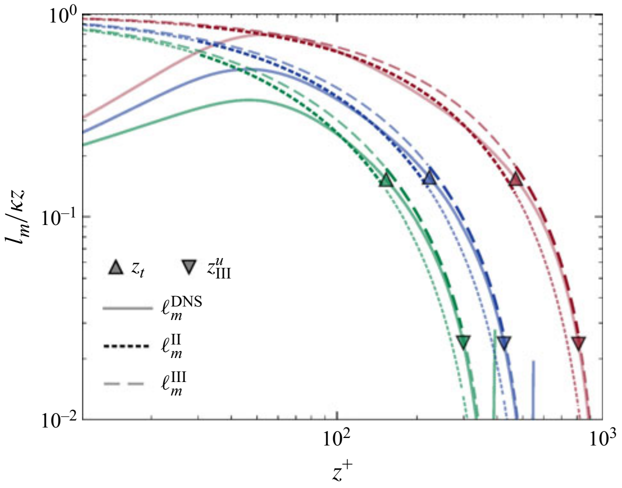

Figure 5. Comparison of the mixing length obtained from DNS ($\ell_m^{DNS} = (-\overline{u'w'})^{1/2}/(\mathrm{d}\overline{u}/\mathrm{d}z)$, solid lines) with the mixing lengths used in this study. The short dashed lines correspond to the mixing length expression for the shear-dominated sublayer, ℓ_m^{II} (5.2), while the long-dashed lines correspond to the mixing length formulation in the stratified outer region, ℓ_m^{III} (5.6). Line colours indicate different cases: green for $Re_\tau = 395$, $Ri_\tau = 720$; blue for $Re_\tau = 550$, $Ri_\tau = 720$; and red for $Re_\tau = 1000$, $Ri_\tau = 600$.

prominent, indicating a transition to a different regime where an alternative mixing length formulation is required.

Substituting the mixing length expression from (5.2) into (5.1) yields the velocitygradient for this region

$$\frac{\mathrm{d}u^+}{\mathrm{d}z^+} = \frac{1}{\kappa z^+}\left(1 + 4.7\frac{z}{\Lambda}\right), \tag{5.3}$$

which we have shown in figure 3 (see short dash-dotted lines, $z/\Lambda < 1$).

Further, upon substituting Λ from (4.2) in (5.3) and integrating, we obtain the velocity profile

$$u^+ = \frac{1}{\kappa}\ln(z^+) + \frac{4.7}{\kappa}\frac{2h}{L}\left(1 - \frac{z}{h}\right)^{-1/2} + C_1, \tag{5.4}$$

where C_1 is the integration constant, obtained by matching (5.4) to the viscous sublayer profile. In neutral conditions, this matching typically occurs at approximately $z^+ \approx 11$ where the viscous and turbulent stresses intersect. With increasing Ri_τ, this point shifts farther away from the wall, as the rate at which turbulent stresses rise is reduced, indicating deeper penetration of buoyancy effects in the near-wall region. This is evident in figure 4(*c*), where the blue curves ($Re_\tau = 550$) show that the darker shades, representing stronger stratification, rise progressively more slowly. Furthermore, for the same $Ri_\tau = 720$, the case at $Re_\tau = 395$ (green) shows an even slower rise compared with $Re_\tau = 550$. This is because the stronger shear tends to resist the suppression of turbulence by buoyancy forces at higher values of Re_τ. The constant used in the present work is described in Appendix A.

Interestingly, the half-channel height, h, appears in (5.4), indicating the influence of an outer length scale on the mean velocity profile near the wall. In the neutral limit ($L \to \infty$), however, this dependence vanishes, and the classical logarithmic law is recovered. With the introduction of stratification, a new length scale Λ emerges, determined by the local stress distribution. This distribution is constrained by the stress boundary conditions at the wall and at the channel centreline, thereby introducing a dependence on h in the formulation.

The shear-dominated sublayer extends from $z^+ \approx 30$ to where stratification effects become prominent relative to the turbulent shear. This transition point can be determined analytically by identifying the location where $z/\varLambda \approx 1$. Substituting $\varLambda = z$ into (4.2) yields

$$\left(\frac{z_t}{h}\right)^3 + \left(\frac{h^2}{L^2} - 3\right)\left(\frac{z_t}{h}\right)^2 + 3\left(\frac{z_t}{h}\right) - 1 = 0, \tag{5.5}$$

whose real root gives the normalised transition location, z_t/h.

For neutral flows, the transition point (z_t) is located at the channel centreline, indicating the absence of buoyancy effects and the dominance of shear throughout the channel. Consequently, the mixing length given by (5.2) is applied up to the channel centre. This assumes a logarithmic law of the wall across the remainder of the neutral velocity profile, which is a reasonable approximation given the relatively weak wake contribution observed in channel flows. With increasing stratification, the transition point shifts closer to the wall, marking the onset of the stratified outer region.

5.2. *Stratified outer region (III)*

This region begins approximately at the transition point ($z = z_t$), beyond which turbulent stresses keep decreasing while still dominating the stress budget (figure 4). Yet, the influence of buoyancy forces becomes increasingly significant ($z/\varLambda > 1$), with large eddying motion being more effectively suppressed. In this region, (5.1) remains valid since turbulent stresses remain much larger than viscous stresses.

However, the mixing length in this region (ℓ_m^{III}) differs from that in the shear-dominated sublayer, as stratification effects become significant ($z/\varLambda > 1$). In this case, ℓ_m^N is normalised using the Businger relation that is corrected by a factor $(1 - z/h)^{1/2}$. As discussed in § 2, similar corrections with varying exponents have been used in previous studies (e.g. Yokoyama *et al.* (1979), Sorbjan (1986)) to extend (1.1) across the ABL. Here, the correction is applied directly to the Businger relation and is motivated by the trends observed in figure 3. Thus,

$$\ell_m^{\mathrm{III}} = \frac{\ell_m^N}{1 + 4.7\zeta}\left(1 - \frac{z}{h}\right)^{-1/2} = \frac{\kappa z}{1 + 4.7\zeta}. \tag{5.6}$$

This mixing length model is also depicted in figure 5 (long dashed lines), agreeing well with the DNS data. The formulation in (5.6) reasonably captures the DNS trend in the region dominated by buoyancy effects.

Substituting (5.6) in (5.1) gives the velocity gradient in the stratified outer region

$$\frac{\mathrm{d}u^+}{\mathrm{d}z} = \frac{1}{\kappa z}\left(1 + 4.7\frac{z}{\varLambda}\right)\left(1 - \frac{z}{h}\right)^{1/2}, \tag{5.7}$$

which, after substituting the definition of $\varLambda$ from (4.2) and integrating, yields the velocity profile

$$u^+ = \frac{1}{\kappa}\ln\frac{z}{h} - \frac{4.7}{\kappa}\frac{h}{L}\ln\left(1 - \frac{z}{h}\right) + \frac{2}{\kappa}\sqrt{1 - \frac{z}{h}} - \frac{2}{\kappa}\ln\left(1 + \sqrt{1 - \frac{z}{h}}\right) + C_2, \tag{5.8}$$

with C_2, being an integration constant. Note that a similar expression was derived for open-channel flows by van de Wiel *et al.* (2012), Donda *et al.* (2015) in the context of ABL.

Furthermore, we observe that C_2 approximately corresponds to the centreline velocity of neutral flows at a given Re_τ, i.e. $C_2 \approx 1/\kappa \ln Re_\tau + 5.2$. This can be reconciled by noting that, in neutral limit ($L \to \infty$), the shear-dominated sublayer extends up to the centreline. Consequently, the stratified outer region reduces to a single point at $z = h$. In this limit, (5.8) yields the centreline velocity of the neutral flow. Note also that, in this case, the buoyancy-related term in (5.8) vanishes, and in the overlap region ($0 \ll z \ll h$) the expression also recovers the classical velocity defect law (Pope 2000), demonstrating the consistency of the approach.

The profile described by (5.8) results from integrating only the turbulent stress contribution (5.1). However, farther from the walls, turbulent stresses gradually become comparable to viscous stresses, and the latter must also be taken into account (see also figure 4). Based on observations across a wide range of cases, this transition typically occurs at a location where $z/\Lambda \approx 8$. This location also marks the upper bound beyond which z/Λ ceases to be a relevant parameter, as the turbulent momentum flux is no longer accurately represented by the total stress in the definition of Λ. Beyond this, (5.1) is no longer valid, marking the onset of the transition layer. Within the turbulent–viscous transition layer, the viscous and turbulent diffusion play comparable roles. Due to the limited extent of this region, a simple linear blending of the adjacent layers provides a reasonable estimate of the flow velocity here. While this blending approach is not explicitly discussed in the main text, its implementation and resulting composite profile are illustrated in Appendix D and also the accompanying Jupyter notebook.

5.3. *Viscous core (V)*

Finally, towards the centre of the channel, stratification may become so influential that the eddies are fully suppressed, turbulence ceases to exist and the local flow is laminar. Since only viscous stresses contribute to the momentum balance in this region, (4.3) simplifies and can be integrated, with the centreline velocity (u^+_{cl}) appearing as the constant of integration

$$\frac{h}{Re_\tau}\frac{\mathrm{d}u^+}{\mathrm{d}z} = 1 - \frac{z}{h}, \qquad u^+_{cl} - u^+ = \frac{Re_\tau}{2}\left(1 - \frac{z}{h}\right)^2. \tag{5.9}$$

The distance from the centreline where the viscous and turbulent stresses become comparable can be estimated as the location up to which the mean velocity follows a parabolic profile. A reasonable estimate for this distance, from the channel centre, is where $h/Re_\tau \sim 2\ell_m\sqrt{\tau/\tau_w}$ (see Appendix B). This point (z^l_{V}) marks the beginning of the viscous core, which extends up to the centreline. If the flow is strongly stratified, then the turbulent stresses vanish earlier, as can be seen in figure 4(*d*). The estimated distance is given as

$$1 - \frac{z^l_{\mathrm{V}}}{h} = \frac{1}{\sqrt{Re_L}}\sqrt{\frac{4.7}{2\kappa}}, \tag{5.10}$$

where $Re_L = u_\tau L/\nu$ is the friction Reynolds number based on the Obukhov length scale.

5.4. *Important parameterisations for predicting the mean velocity profile*

The velocity profiles ((5.4), (5.8), (5.9)) depend on the governing input parameters Re_τ and Ri_τ. Yet, an important parameter naturally emerging throughout the analysis is a Richardson number based on wall fluxes, $Ri_w = h/L$ (recall 1.1). Hence, to obtain a closed

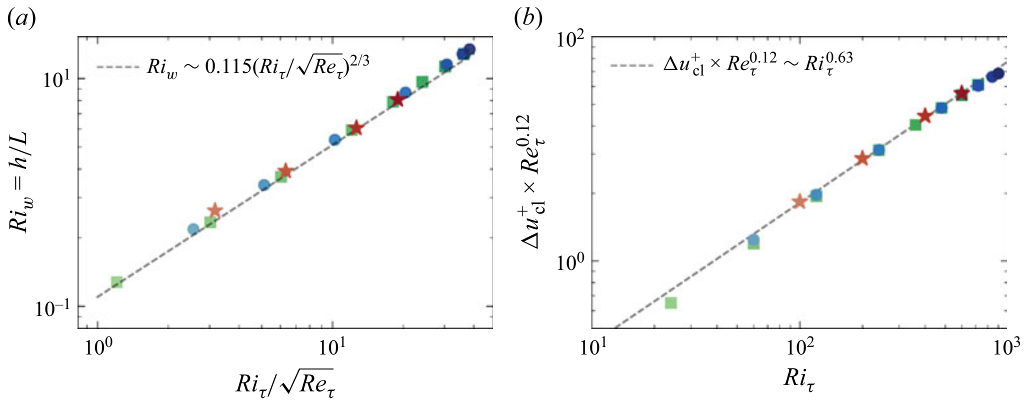

Figure 6. (*a*) The proposed scaling to estimate *a priori* the parameter $Ri_w = h/L$. (*b*) Parametrisation of the deviation of the centreline velocity from the neutral case at same Re_τ. Increasing darkness of the marker colours denotes increasing Richardson numbers. The symbols and colours are as indicated in figure 2.

form of the velocity profiles, Ri_w must be estimated *a priori*. To this end, we derive a relation (see Appendix C) for it in terms of Re_τ and Ri_τ, relying on the Nusselt number scaling proposed by Zonta *et al.* (2022) that was obtained for a range of cases (either simulated at $Pr = 0.71$ or rescaled accordingly). The proposed scaling is given by

$$Ri_w = \frac{h}{L} = \frac{\kappa\ (g/\theta_0)\ q_w}{u_\tau^3/h} \sim \left(\frac{Ri_\tau}{\sqrt{Re_\tau}}\right)^{2/3}. \tag{5.11}$$

Figure 6(*a*) shows the agreement of this scaling for the different cases considered in this study. Additionally, the viscous core solution requires a closure for stratification effects on the centreline velocity, u^+_{cl}. This is done by modelling its deviation from the neutral case at the same Re_τ, given by $u^+_{cl,N} \approx 1/\kappa \ln Re_\tau + 5.2$. With stratification, turbulence suppression near the centreline leads to an increased u^+_{cl} that we found to be well captured by

$$\Delta u^+_{cl} = u^+_{cl} - u^+_{cl,N} = Ri_\tau^{0.63} Re_\tau^{-0.12}, \tag{5.12}$$

as shown in figure 6(*b*). Indeed, Δu^+_{cl} increases with Ri_τ as expected due to stronger stratification effects, and depends weakly on Re_τ, as most of its influence is already accountedfor in $u^+_{cl,N}$.

These parametric relations and ((5.4), (5.8), (5.9)) are the ingredients needed for reconstructing the mean velocity profile across the entire channel height. In the following section, we compare the predictions against our DNS dataset to evaluate the applicability of MOST in this confined flow configuration.

6. Assessment of the proposed scaling with DNS

Figure 7 compares the composite mean velocity profile predicted by the proposed approach against DNS results across several Re_τ and Ri_τ cases. The profiles, plotted in linear coordinates from the wall to the channel centreline, provide a global assessment of the model performance. The individual contributions from ((5.4), (5.8), (5.9)) are shown as dashed lines, with the highlighted segments indicating the region over which each

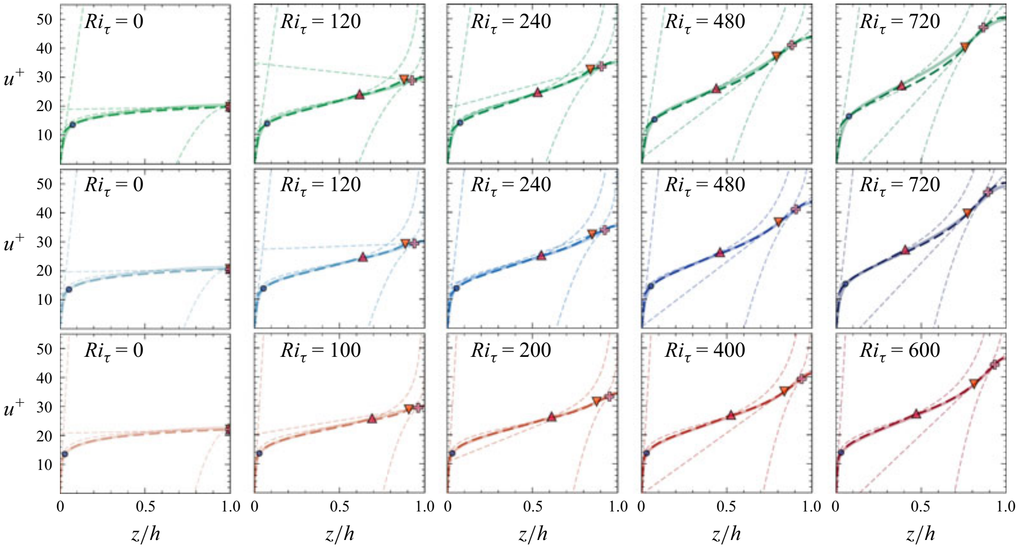

Figure 7. The composite mean velocity profiles obtained from the proposed formulation (dashed lines) are compared with DNS data (solid lines). The markers indicate the boundaries of the different regions, as defined in figure 4. Results are shown for $Re_\tau = 395$ (greens), $Re_\tau = 550$ (blues) and $Re_\tau = 1000$ (reds). The implementation of the mean velocity profile reconstruction and the estimation of the skin-friction coefficient can be found in this notebook.

expression is valid. The symbols are used to distinguish the different flow regions discussed earlier.

In addition to this overall comparison, figure 8 offers a closer picture of the predicted and DNS velocity profiles, focusing on the different flow regions. To examine the influence of stratification, results are presented for flows with $Ri_\tau = 0,\ 60,\ 240$ and 720 at $Re_\tau = 550$ (shown in increasingly darker shades of blue). Moreover, to compare the Reynolds number effects, results for flows with $Ri_\tau = 720$ are presented at $Re_\tau = 395,\ 550$ (green, dark blue). Since the case at $Ri_\tau = 720$ was unavailable for $Re_\tau = 1000$, the result of the closest available $Ri_\tau = 600$ is shown in dark red.

In the shear-dominated sublayer (II), it can be observed that (5.4) accurately predicts the mean velocity profile with discrepancies appearing only for strongly stratified flows; for instance, $Ri_\tau = 720$ at $Re_\tau = 395$ (figure 8*a*). This is due to insufficient scale separation in the flow, particularly at the imposed stratification. When Re_τ is not sufficiently large and stratification is strong, the smallest eddies in the flow are not small enough to remain unaffected by buoyancy. As a result, a substantial portion of the turbulence spectrum is suppressed. The estimated extent of the shear-dominated sublayer (z_t) is indicated for different cases with ▲. If $z_t^+ < 150$, then the buoyancy effects are perceived too close to the wall, disrupting the near-wall region of the flow and thus violating the assumption of a logarithmic velocity profile in this region.

In the stratified outer region (III), predictions with (5.8), with $C_2 \approx 1/\kappa \ln Re_\tau + 5.2$, agree well with all the cases except for the case at $Re_\tau = 395$ (figure 8*b*), for the same reason as described above. While the equation effectively reproduces the general shape of the velocity profile, we observe a shift for low Re_τ cases. The point marked with ▼ (z^u_{III}) in figure 8(*b*) indicates the end of the stratified outer region and the onset of the turbulent-viscous transition layer, where the influence of viscous stresses becomes comparable to that of turbulent stresses. Finally, figure 8(*c*) also confirms the agreement of the parabolic

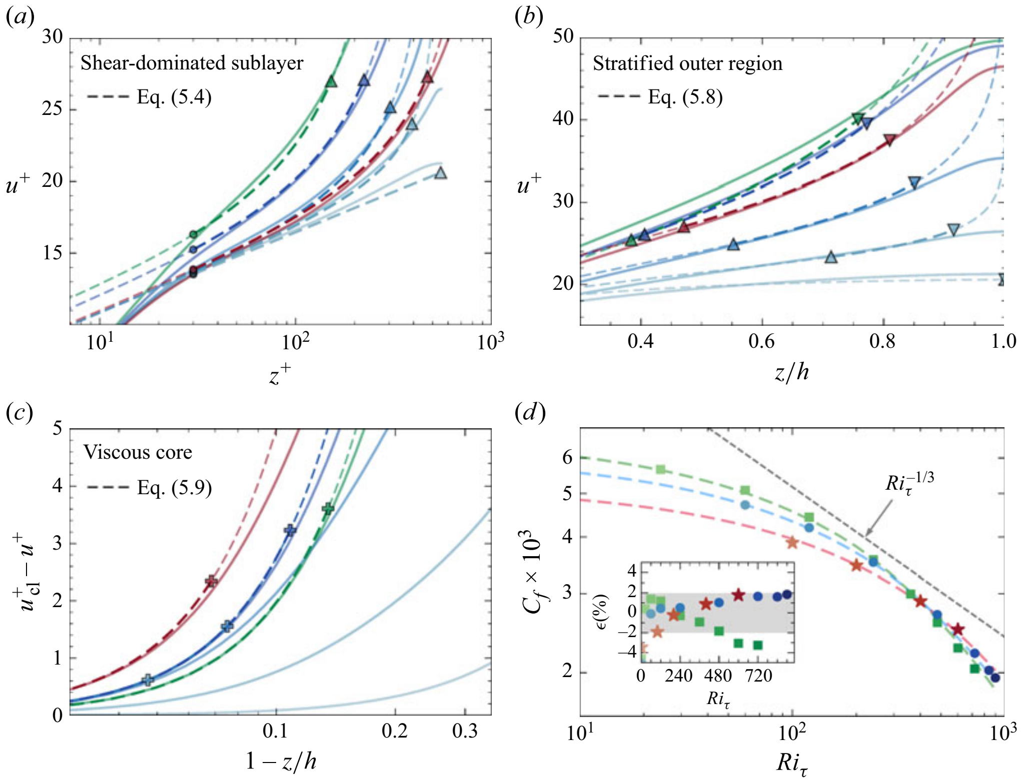

Figure 8. Mean streamwise velocity profiles in stably stratified turbulent channel flows. The solid lines correspond to DNS data which are compared against (*a*) (5.4) in the shear-dominated sublayer, (*b*) (5.8) in the stratified outer region and (*c*) (5.9) in the viscous core. The predictions are indicated with dashed lines. Blue curves: $Re_\tau = 550$, $Ri_\tau = 0,\ 60,\ 240,\ 720$ (increasing darkness). Green: $Re_\tau = 395$, $Ri_\tau = 720$. Red: $Re_\tau = 1000$, $Ri_\tau = 600$. Symbols ▲, ▼ and ✚ indicate the bounds of different regions. (*d*) Comparison of skin-friction coefficient, C_f, predicted by the proposed approach (coloured dashed lines) with DNS data (symbols) as a function of Ri_τ. The grey dashed line indicates the $C_f \sim Ri_\tau^{-1/3}$ scaling shown in Zonta *et al.* (2022). The inset shows the percentage error (ϵ) between the model and DNSs at different Ri_τ across all cases considered. The shaded region indicates a ±2 % error band. The implementation of the mean velocity profile reconstruction and the estimation of the skin-friction coefficient can be found in this notebook.

velocity profile with DNS data in the viscous core (V). The velocity profile in this region follows a parabolic form parametrised solely by Re_τ. Hence, a distinct parabolic curve is obtained for each $Re_\tau = 395,\ 550,\ 1000$. The extent to which the DNS profiles follow the parabolic form, measured from the channel centre, increases with stratification. This is evident for $Ri_\tau = 0,\ 60,\ 240,\ 720$ (increasing shades of blue) at $Re_\tau = 550$. Specifically, the $Ri_\tau = 720$ case follows the parabolic profile over a larger portion of the core compared with $Ri_\tau = 60$ and 240, while $Ri_\tau = 0$ does not exhibit this behaviour in the centre. The boundary marking the approximate location beyond which the velocity profiles begin to diverge from the parabola is indicated by the symbol ✚. We observe that, for $Ri_\tau = 720$ at $Re_\tau = 395,\ 550$ and $Ri_\tau = 600$ at $Re_\tau = 1000$, this is estimated reasonably well. However, at lower Ri_τ values, corresponding to $Re_\tau = 550$, this boundary is estimated to be at a slightly larger distance from the channel centre than the actual location where the velocity profiles begin to diverge from the parabola. Nevertheless, this difference is visually exaggerated due to the logarithmic horizontal axis, and the estimate is acceptable for practical purposes.

The mean velocity profile obtained from the proposed approach can be integrated to obtain bulk velocity (u_b), and consequently estimate the skin-friction coefficient ($C_f = 2\tau_w/\rho u_b^2 = 2/u_b^{+2}$). Figure 8(*d*) compares these estimates with values obtained from DNS, with the scaling $C_f \sim Ri_\tau^{-1/3}$ reported by Zonta *et al.* (2022) also shown for reference. While this relation may hold in a narrower parameter range, it tends to deviate from DNS results over the wider parameter space explored in this study. Integrating the velocity profile obtained from the proposed approach yields consistently accurate results, illustrating the robustness of the present framework. The relative errors, defined as $\epsilon = (C_f^{DNS} - C_f)/C_f^{DNS}$, are generally within a 2 % margin, with the exception of the high Ri_τ cases at the lowest $Re_\tau = 395$, where deviations up to 4 % are observed. This slightly larger error is, once more, an expected consequence of the lack of scale separation in these cases.

7. Conclusion

In this work, we have leveraged a framework derived for atmospheric science – MOST – and adopted it to describe the mean velocity in a stably stratified turbulent internal (channel) flow. The linear Businger relation is employed as the stability correction function to characterise the effect of stable stratification on the mean velocity profile. Based on the relative contributions of viscous and turbulent stresses and the local stability parameter (z/Λ), distinct flow regions were identified. The classical viscous sublayer is followed by a shear-dominated sublayer, where the mean flow is properly characterised by wall values and stratification effects are minimal. This is followed by a stratified outer region extending from $z \approx \Lambda(z)$ to $z \approx 8\Lambda(z)$. Turbulent stresses then become comparable to the viscous stresses in the turbulent-viscous transition layer. Finally, the flow becomes laminar in the viscous core, whose onset was estimated to scale inversely with ($Re_L^{-1/2}$). In the analysis, the wall Richardson number, $Ri_w = h/L$, and deviation from the neutral centreline velocity, Δu_{cl}^+, emerge as important parameters. Accordingly, we have proposed parametric relations to estimate them that enable an accurate reconstruction of the mean velocity profile for a wide range of governing parameters Re_τ and Ri_τ. Our findings highlight MOST's robustness by demonstrating that a theory originally developed and validated for atmospheric flows at scales of ∼100 m effectively extends to stably stratified turbulence in internal flows, applicable in systems at scales orders of magnitude smaller (e.g. ∼0.01 m). The framework effectively captures stratification effects despite relying on empirical, non-universal stability correction functions. Crucially, the reconstructed profiles enable a reliable estimation of the skin-friction coefficient, with errors generally within 3 %. This provides a framework for quantifying pressure losses, offering practical value for modelling and designing flow systems in engineering applications where stratification is important.

Acknowledgements. We thank Baptiste Hardy for valuable discussions on MOST and stably stratified turbulent boundary layers. We are also grateful for the fruitful exchanges with Giandomenico Lupo and Asif Hasan. We further thank Dr. Francesco Zonta for providing DNS data. This work was supported by the European Research Council (grant no. ERC-2019-CoG-864660, Critical), and NVIDIA Corporation (Academic Grant Turbulent forced convection beyond the Oberbeck-Boussinesq hypothesis).

Funding. Open access funding provided by Delft University of Technology.

Declaration of Interests. The authors report no conflict of interest.

Appendix A. Velocity profile in shear-dominated sublayer

In this section, we elaborate on the shear-dominated sublayer (introduced in § 5.1 in the main text), with particular focus on estimating the constant of integration in the velocity profile expression.

In the shear-dominated sublayer, the total stress is dominated by turbulent shear stress, which can be approximated by the wall shear stress. This forms the basis for deriving the mean velocity profile in this region, as outlined below

$$\ell_m \frac{\mathrm{d}\overline{u}}{\mathrm{d}z} = u_\tau \left(1 - \frac{z}{h}\right)^{1/2}, \tag{A1}$$

where ℓ_m in region II is formulated using ℓ_m^N (4.5), and the Businger relation as

$$\ell_m^{\mathrm{II}} = \frac{\ell_m^N}{\phi} = \frac{\ell_m^N}{1 + 4.7\,\zeta} = \frac{\kappa z}{1 + 4.7\,\zeta}\left(1 - \frac{z}{h}\right)^{1/2}; \qquad \zeta = \frac{z}{\Lambda}. \tag{A2}$$

We also know that

$$\Lambda = L\left(1 - \frac{z}{h}\right)^{3/2}. \tag{A3}$$

Using (A3) and integrating the gradient yields the velocity profile in the shear-dominated sublayer

$$u^+ = \frac{1}{\kappa}\ln z^+ + \frac{4.7}{\kappa}\frac{2h}{L}\left(1 - \frac{z}{h}\right)^{-1/2} + C_0, \tag{A4}$$

where C_0 is a constant. As indicated in the main text, the constant is determined by matching the profiles between the viscous and shear-dominated sublayers. For instance, if the linear profile, $u^+ = z^+$, is matched with (A4) at $z^+ = z_M^+$ then the constant C_0 is given as

$$C_0 = z_M^+ - \frac{1}{\kappa}\ln(z_M^+) - \frac{4.7}{\kappa}\frac{2h}{L} - \frac{4.7}{\kappa}\frac{h}{L}\frac{z_M^+}{Re_\tau}, \tag{A5}$$

where the position z_M^+ is defined as

$$z_M^+ = 11.1 + C_z \max\left(0, \frac{Ri_\tau}{Re_\tau} - 0.5\right), \tag{A6}$$

with $C_z = 2$ used in the present work.

In neutral flows, the matching occurs at $z_M^+ = 11.1$. For stably stratified flows, the constant C_0 is determined at $z_M^+ = 11.1$ for $Ri_\tau/Re_\tau < 0.5$, beyond which the intersection point was observed to scale linearly with stratification strength. The value of 0.5 is based on observations. The slope, C_z, may depend on Re_τ, but precise determination of the function would require a significantly larger dataset. While other functional forms of z_M^+ could also be used to fit the data, the primary focus here is on the conceptual framework and formulation rather than a detailed empirical fit.

Appendix B. Extent of the viscous core

This section provides additional details on the estimation of the transition point z_{V}^l discussed in § 5.3 (Viscous core (V)) of the main manuscript.

The mean shear can be evaluated as the root of the quadratic streamwise momentum balance equation

$$\frac{\mathrm{d}u^+}{\mathrm{d}z} = \frac{2\tau/\tau_w}{\dfrac{h}{Re_\tau} + \sqrt{\dfrac{h^2}{Re_\tau^2} + 4l_m^2\dfrac{\tau}{\tau_w}}}. \tag{B1}$$

In the viscous core, turbulent stresses vanish, and viscous diffusion is the only mechanism of momentum transport, implying that $4l_m^2\tau/\tau_w = 0$, in the above equation. However, moving away from the channel centreline, viscous stresses gradually give in to turbulent stresses. The location where these two contributions become comparable marks the point at which turbulent stresses start to dominate the flow dynamics

$$\frac{h}{Re_\tau} \sim 2l_m\sqrt{\frac{\tau}{\tau_w}} \quad \text{where,} \quad l_m = \kappa z\left(1 + 4.7\frac{z}{\Lambda}\right)^{-1}. \tag{B2}$$

In the limit, $z \to h$, $\Lambda \to 0$, therefore

$$l_m \sim \frac{\kappa\Lambda}{4.7} \sim \frac{\kappa L}{4.7}\left(1 - \frac{z}{h}\right)^{3/2}. \tag{B3}$$

Using this in (B2)

$$\frac{h}{Re_\tau} \sim 2\frac{\kappa L}{4.7}\left(1 - \frac{z}{h}\right)^2. \tag{B4}$$

The wall-normal distance that marks the extent of the viscous core is denoted by z_V^l

$$1 - \frac{z_V^l}{h} \sim \sqrt{\frac{4.7}{2\kappa}}\sqrt{\frac{h}{L}}\sqrt{\frac{1}{Re_\tau}}. \tag{B5}$$

Appendix C. Parametrisation of wall Richardson number (*Ri*$_w = h/L$)

This section outlines the step-by-step derivation of the parametric relation used in the main text to express the Obukhov length scale in terms of Re_τ and Ri_τ ((5.11) in the main text). Consider the definition of the Obukhov length scale

$$L = \frac{u_\tau^3}{\kappa(g/\theta_0)q_w}; \quad \text{where, } q_w = \alpha\left.\frac{\mathrm{d}\overline{\theta}}{\mathrm{d}z}\right|_w = \frac{\nu}{Pr}\left.\frac{\mathrm{d}\overline{\theta}}{\mathrm{d}z}\right|_w \tag{C1}$$

$$\Longrightarrow \frac{h}{L} = h\,\frac{\kappa(g/\theta_0)q_w}{u_\tau^3} = \kappa\; h\;\frac{g}{\theta_0}\;\frac{1}{u_\tau^3}\;\frac{\nu}{Pr}\left.\frac{\mathrm{d}\overline{\theta}}{\mathrm{d}z}\right|_w, \tag{C2}$$

where Pr is the Prandtl number of the flow. Multiplying and dividing by h and $\Delta\rho/\rho_0$, and grouping terms corresponding to Re_τ and Ri_τ

$$\frac{h}{L} \sim \frac{h}{\theta_0}\;\frac{\rho_0}{\Delta\rho}\;\frac{\Delta\rho g h}{\rho_0 u_\tau^2}\;\frac{\nu}{u_\tau h}\;\frac{1}{Pr}\left.\frac{\mathrm{d}\overline{\theta}}{\mathrm{d}z}\right|_w. \tag{C3}$$

We also use the ideal gas relation, $\Delta\rho/\rho_0 = \Delta\theta/\theta_0$

$$\frac{h}{L} \sim \frac{1}{Pr}\;\frac{Ri_\tau}{Re_\tau}\;\frac{h}{\Delta\theta}\left.\frac{\mathrm{d}\overline{\theta}}{\mathrm{d}z}\right|_w. \tag{C4}$$

From Zonta *et al.* (2022)

$$Nu \sim \left(\frac{Re_\tau^2}{Ri_\tau}\right)^{1/3}; \quad \text{where,} \quad Nu = \frac{2q_w h}{\lambda \Delta\theta} \sim \frac{h}{\Delta\theta} \left.\frac{\mathrm{d}\overline{\theta}}{\mathrm{d}z}\right|_w. \tag{C5}$$

Substituting this in the h/L relation (note that $Ri_w = h/L$ is termed a Richardson number because it can be expressed in a conventional form that denotes the relative importance of turbulence destruction by buoyancy forces and turbulence production)

$$Ri_w = \frac{\kappa\ (g/\theta_0)\ q_w}{u_\tau^3/h} = \frac{h}{L} \sim \frac{1}{Pr}\left(\frac{Ri_\tau}{\sqrt{Re_\tau}}\right)^{2/3}. \tag{C6}$$

It is important to note that, although the Prandtl number (Pr) appears in this analysis, its explicit role in the derivation of Zonta *et al.*'s relation remains unclear. In this study, all of the results are presented for constant $Pr = 0.71$. Moreover, the applicability of MOST across a broad range of Pr values has not been thoroughly examined and requires a dedicated investigation beyond the scope of this work.

Appendix D. Composite mean velocity profile

The mean velocity profiles in the viscous sublayer, shear-dominated sublayer, stratified outer region and the viscous core are described in ((5.4), (5.8), (5.9)), respectively. To obtain the composite mean velocity profile across the entire channel, the velocity in the turbulent–viscous transition layer must be determined. This is achieved by smoothly blending the velocity profiles from the adjacent regions. If u_{III} and u_{V} denote the predicted velocities in regions III and V, then the velocity profile in region IV is

$$u_{\mathrm{IV}} = \gamma\ u_{\mathrm{III}} + (1-\gamma)\ u_{\mathrm{V}}; \quad \text{where,} \quad \gamma = \frac{z_{\mathrm{V}}^l - z}{z_{\mathrm{V}}^l - z_{\mathrm{III}}^u}. \tag{D1}$$

Here, z_{III}^u and z_{V}^l are the upper and lower bounds of regions III and V, respectively.

REFERENCES

ARMENIO, V. & SARKAR, S. 2002 An investigation of stably stratified turbulent channel flow using large-eddy simulation. *J. Fluid Mech.* **459**, 1–42.

BELJAARS, A.C.M. & HOLTSLAG, A.A.M. 1991 Flux parameterization over land surfaces for atmospheric models. *J. Appl. Meteorol. Climatol.* **30** (3), 327–341.

BRETHOUWER, G., BILLANT, P., LINDBORG, E. & CHOMAZ, J.-M. 2007 Scaling analysis and simulation of strongly stratified turbulent flows. *J. Fluid Mech.* **585**, 343–368.

BUSINGER, J. & YAGLOM, A. 1971 Introduction to Obukhov's paper on turbulence in an atmosphere with a non-uniform temperature. *Boundary-Layer Meteorol.* **2**, 3–6.

CAULFIELD, C.P. 2021 Layering, instabilities, and mixing in turbulent stratified flows. *Annu. Rev. Fluid Mech.* **53** (1), 113–145.

CHENGE, Y. & BRUTSAERT, W. 2005 Flux-profile relationships for wind speed and temperature in the stable atmospheric boundary layer. *Boundary-Layer Meteorol.* **114** (3), 519–538.

COOK, A.W. & RILEY, J.J. 1996 Direct numerical simulation of a turbulent reactive plume on a parallel computer. *J. Comput. Phys.* **129** (2), 263–283.

COSTA, P. 2018 A FFT-based finite-difference solver for massively-parallel direct numerical simulations of turbulent flows. *Comput. Math. Appl.* **76** (8), 1853–1862.

DONDA, J.M.M., VAN HOOIJDONK, I.G.S., MOENE, A.F., JONKER, H.J.J., VAN HEIJST, G.J.F., CLERCX, H.J.H. & VAN DE WIEL, B.J.H. 2015 Collapse of turbulence in stably stratified channel flow: a transient phenomenon. *Q. J. R. Meteorol. Soc.* **141** (691), 2137–2147.

DYER, A.J. 1974 A review of flux-profile relationships. *Boundary-Layer Meteorol.* **7** (3), 363–372.

FUKUI, K., NAKAJIMA, M. & UEDA, H. 1983 A laboratory experiment on momentum and heat transfer in the stratified surface layer. *Q. J. R. Meteorol. Soc.* **109** (461), 661–676.

GARCIA-VILLALBA, M. & DEL ALAMO, J.C. 2011 Turbulence modification by stable stratification in channel flow. *Phys. Fluids* **23** (4), 045104.

GARG, R.P., FERZIGER, J.H., MONISMITH, S.G. & KOSEFF, J.R. 2000 Stably stratified turbulent channel flows. i. stratification regimes and turbulence suppression mechanism. *Phys. Fluids* **12** (10), 2569–2594.

GRACHEV, A.A., ANDREAS, E.L., FAIRALL, C.W., GUEST, P.S. & PERSSON, P.O.G. 2015 Similarity theory based on the Dougherty–Ozmidov length scale. *Q. J. R. Meteorol. Soc.* **141** (690), 1845–1856.

GRYNING, S.-E., BATCHVAROVA, E., BRÜMMER, B., JØRGENSEN, H. & LARSEN, S. 2007 On the extension of the wind profile over homogeneous terrain beyond the surface boundary layer. *Boundary-Layer Meteorol.* **124** (2), 251–268.

HOLTSLAG, A.A.M. & NIEUWSTADT, F.T.M. 1986 Scaling the atmospheric boundary layer. *Boundary-Layer Meteorol.* **36** (1), 201–209.

IIDA, O., KASAGI, N. & NAGANO, Y. 2002 Direct numerical simulation of turbulent channel flow under stable density stratification. *Intl J. Heat Mass Transfer* **45** (8), 1693–1703.

LI, D., SALESKY, S.T. & BANERJEE, T. 2016 Connections between the Ozmidov scale and mean velocity profile in stably stratified atmospheric surface layers. *J. Fluid Mech.* **797**, R3.

MAJDA, A. & SETHIAN, J. 1985 The derivation and numerical solution of the equations for zero mach number combustion. *Combust. Sci. Technol.* **42** (3–4), 185–205.

MOESTAM, R. & DAVIDSON, L. 2005 Numerical simulations of a thermocline in a pressure-driven flow between two infinite horizontal plates. *Phys. Fluids* **17** (7), 075109.

MONIN, A. & OBUKHOV, A. 1954 Basic laws of turbulent mixing in the surface layer of the atmosphere, 163–187.

NIEUWSTADT, F.T.M. 1984 The turbulent structure of the stable, nocturnal boundary layer. *J. Atmos. Sci.* **41** (14), 2202–2216.

NIEUWSTADT, F.T.M. 2005 Direct numerical simulation of stable channel flow at large stability. *Boundary-Layer Meteorol.* **116** (2), 277–299.

OBUKHOV, A. 1971 Turbulence in an atmosphere with a non-uniform temperature. *Boundary-Layer Meteorol.* **2** (1), 7–29.

PIROZZOLI, S. 2014 Revisiting the mixing-length hypothesis in the outer part of turbulent wall layers: mean flow and wall friction. *J. Fluid Mech.* **745**, 378–397.

POPE, S.B. 2000 *Turbulent Flows*. Cambridge University Press.

SALESKY, S.T., KATUL, G.G. & CHAMECKI, M. 2013 Buoyancy effects on the integral lengthscales and mean velocity profile in atmospheric surface layer flows. *Phys. Fluids* **25** (10), 105101.

SHEN, Z., LIU, L., LU, X.-Y. & STEVENS, R.J.A.M. 2025 Mean turbulent momentum fluxes and wind deficits in nocturnal stable atmospheric boundary layers. *J. Fluid Mech.* **1017**, A5.

SORBJAN, Z. 1986 On similarity in the atmospheric boundary layer. *Boundary-Layer Meteorol.* **34** (4), 377–397.

STIPERSKI, I. & CALAF, M. 2023 Generalizing Monin–Obukhov similarity theory, 1954 for complex atmospheric turbulence. *Phys. Rev. Lett.* **130** (12), 124001.

VAN DE WIEL, B.J.H., MOENE, A.F. & JONKER, H.J.J. 2012 The cessation of continuous turbulence as precursor of the very stable nocturnal boundary layer. *J. Atmos. Sci.* **69** (11), 3097–3115.

WEBB, E.K. 1970 Profile relationships: the log-linear range, and extension to strong stability. *Q. J. R. Meteorol. Soc.* **96** (407), 67–90.

YOKOYAMA, O., GAMO, M. & YAMAMOTO, S. 1979 The vertical profiles of the turbulence quantities in the atmospheric boundary layer. *J. Meteorol. Soc. Japan Ser.* **57** (3), 264–272.

ZONTA, F., SICHANI, P.H. & SOLDATI, A. 2022 Interaction between thermal stratification and turbulence in channel flow. *J. Fluid Mech.* **945**, A3.

ZONTA, F. & SOLDATI, A. 2018 Stably stratified wall-bo unded turbulence. *Appl. Mech. Rev.* **70** (4), 040801.